Corrections on energy spectrum and scatterings for fast neutron radiography at NECTAR facility *

LIU Shu-Quan(刘树全)[1,2] Bücherl Thomas[2] LI Hang(李航)[1,3]
ZOU Yu-Bin(邹宇斌)[1] LU Yuan-Rong(陆元荣)[1;1)] GUO Zhi-Yu(郭之虞)[1]

[1] State Key Lab of Nuclear Physics and Technology & School of Physics, Peking University, Beijing 100871, China
[2] Technische Universität München, ZTWB Radiochemie München RCM, Walther-Meissner-Str. 3, Garching 85748, Germany
[3] Institute of Nuclear Physics and Chemistry, Chinese Academy of Engineering Physics, Mianyang 621900, China

Abstract: Distortions caused by the neutron spectrum and scattered neutrons are major problems in fast neutron radiography and should be considered for improving the image quality. This paper puts emphasis on the removal of these image distortions and deviations for fast neutron radiography performed at the NECTAR facility of the research reactor FRM-II in Technische Universität München (TUM), Germany. The NECTAR energy spectrum is analyzed and established to modify the influence caused by the neutron spectrum, and the Point Scattered Function (PScF) simulated by the Monte-Carlo program MCNPX is used to evaluate scattering effects from the object and improve image quality. Good analysis results prove the sound effects of the above two corrections.

Key words: fast neutron radiography, correction, energy spectrum, scattering, NECTAR

PACS: 28.20.Cz, 81.70, 83.85.Hf **DOI:** 10.1088/1674-1137/37/11/118201

1 Introduction

Fast neutron radiography is a suitable detection tool for bulk objects due to the low cross-section of fast neutrons and the elements. For quantitative analysis, such as the defect evaluations and fast neutron tomography, some significant effects should be considered and corrected [1–3].

1.1 Problems and methods

In traditional radiography analysis, the relationship between the gray values on the image and the sample thickness t is treated by the exponential attenuation law:

$$\frac{I}{I_0}=\mathrm{e}^{\Sigma_{\mathrm{tot}}(E)\cdot t}, \tag{1}$$

where $\Sigma_{\mathrm{tot}}(E)$ is the linear attenuation coefficient of the sample as a function of neutron energy E, and I_0 and I are the neutron flux before and after the penetration. Usually a constant Σ_{tot} will be used to evaluate the sample thickness, but this will bring in deviations when the neutron beams are polychromatic. This is called the energy spectrum effects in fast neutron radiography [4].

The scattering effects, on the other hand, are mainly caused by the interacted neutrons scattered out from the sample, which make overlaps and blurring on the images. Neutrons recorded on the detectors can be represented as the sum of penetrated neutrons and scattered neutrons I_{s}. Our goal is to evaluate and remove I_{s} from the original images I. Fig. 1 shows the ratios of scattering cross-section to total cross-section ($\sigma_{\mathrm{s}}/\sigma_{\mathrm{t}}$) for different materials at neutron energies between 1.0 and 10 MeV. It is noticed that scattering effects are more significant in fast neutron radiography, as can be seen in Fig. 1 that more than 90% of the attenuated neutrons are scattered during fast neutron radiography.

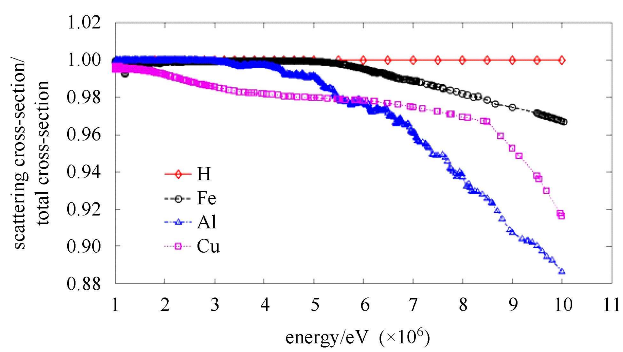

Fig. 1. (color online) Scattering to total cross-section ratios for different elements at fast neutron energies [5].

Received 9 January 2013
∗ Supported by National Natural Science Foundation of China (11079001)
1) E-mail: yrlu@pku.edu.cn

Considering both energy spectrum and scattering effects, Eq. (1) is now fixed as

$$\frac{I-I_{\rm s}}{I_0}=\frac{\int_0^{E_0}\phi(E){\rm e}^{-\Sigma_{\rm tot}(E)t}{\rm d}E}{\int_0^{E_0}\phi(E){\rm d}E}, \tag{2}$$

where $\phi(E)$ is the incident neutron spectrum and $I_{\rm s}$ is the scattered neutron flux detected.

The evaluation of $I_{\rm s}$ in fast neutron radiography is a key problem in corrections. Decades ago the way for evaluating $I_{\rm s}$ was to model the fast neutron experiment conditions and estimate the scattering component with an analytical representation [6–9]. Recently an effective method for scattering correction in thermal neutron radiography is using the Point Scattered Function [10, 11]. However, due to the large-size object used in fast neutron radiography, the simulation of PScFs for fast neutrons is time consuming and requires high CPU performances. In this work, to solve this problem, Linux cluster and parallel computing technology is applied and PScF method is extended to fast neutrons scattering analysis.

These two effects are studied separately by adjusting the samples in this work. The fast neutron spectrum effects were numerically calculated and applied to the image analysis. PScFs of fast neutrons were simulated and integrated by all beams penetrating the sample to obtain $I_{\rm s}$ and then it was subtracted from the original image. The quantitative results with and without each effect will be discussed and compared finally.

1.2 NECTAR facility

This work was performed at the NECTAR (NEutron Computerized Tomography And Radiography) facility located at the research reactor FRM-Ⅱ in Technische Universität München (TUM), Germany [12]. The layouts of NECTAR and experiment conditions are shown in Fig. 2. The source-to-detector distance was L=9355 mm with a neutron beam of divergence 2.1° and average neutron energy of 1.9 MeV. The neutron flux at sample position is 5.4×10^5 cm^{-2}s^{-1} and the L/D ratio is 233. As L and L/D are so large here, parallel beam geometries were used in later calculations. A 300 mm×300 mm×2.4 mm pp-converter (doped with 30% ZnS) with a spatial resolution of 0.6 mm was used as the detector [13]. The sample-to-detector distance was flexible depending on the experimental requirements.

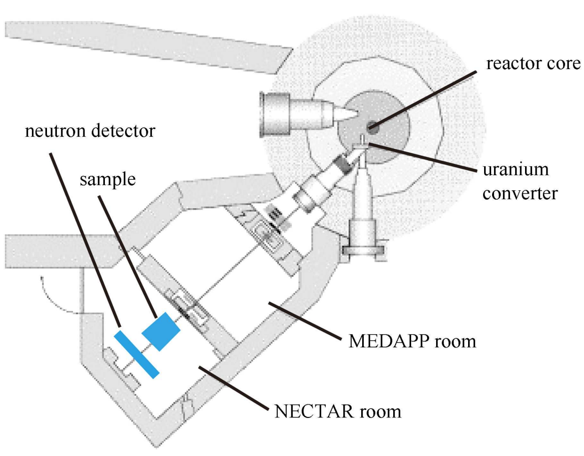

Fig. 2. (color online) Sketch of the fast neutron radiography experiment conditions at NECTAR [12].

2 Energy spectrum effects

2.1 Analysis

Considering the neutron energy spectrum of NECTAR, the expression of ln (I/I_0) and t treated from Eq. (2) is now:

$$-\ln\left(\frac{I}{I_0}\right)=-\ln\left(\frac{\int_0^{E_0}\phi(E){\rm e}^{-\Sigma_{\rm tot}(E)t}{\rm d}E}{\int_0^{E_0}\phi(E){\rm d}E}\right). \tag{3}$$

For monochromatic neutrons the linear attenuation coefficient $\Sigma_{\rm tot}(E)$ is independent of energy E thus ln (I/I_0) have a linear relationship with thickness t. For polychromatic neutrons the right side of Eq. (3) was numerically integrated and fitted by polynomial representations.

Figure 3 shows the relationships of $-\ln(I/I_0)$ and penetrating depth t with and without the energy spectrum effects. It can be seen that below 14 cm thickness, the polychromatic neutron beam attenuates faster than monochromatic neutrons. This is due to the thermal neutron components in the beam at NECTAR, which has larger cross-sections of iron and attenuates faster. However, when t is larger than 14 cm, less thermal neutrons and relatively more fast neutrons remain in the beams, which makes the beam attenuate slowly.

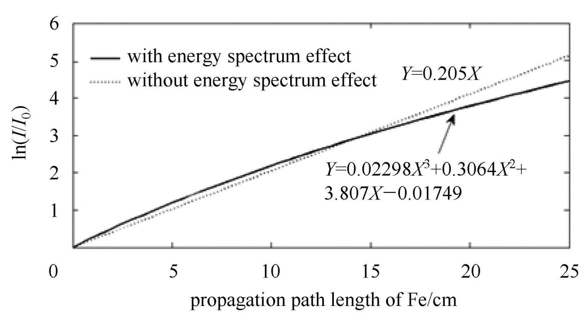

Fig. 3. (color online) The relationship between $\ln(I/I_0)$ and penetrating depth t of iron with and without the NECTAR energy spectrum effect. Polynomial fittings are also shown in the figure.

2.2 Experiment and results

A group of three iron cylinders with air drillings was used to check the neutron energy spectrum effects at NECTAR (Fig. 4). The outer and inner diameters of cylinder 1, 2, 3 are: 7.0(2.0), 8.0(3.2) and 8.0(6.2) cm, respectively. To avoid other effects, iron was selected because iron has a relatively low scattering cross-section for fast neutrons compared to other materials. The distance of the center of sample group 1 to detector was set to 380 mm so that the sample scatterings can be ignored.

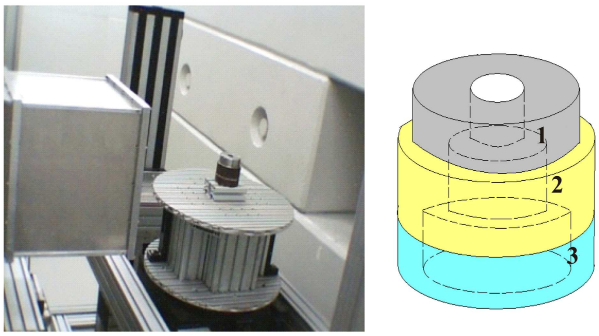

Fig. 4. (color online) Sample group 1. Left: Experiment arrangement for sample group 1 in NECTAR platform; Right: Geometry diagram of sample group 1.

The raw image was filtered, processed by open beam image, dark image and finally normalized as shown in Fig. 5. Three lines were drawn crossing the three cylinders and the line data were obtained as three arrays for quantitative analysis.

Figure 6 shows the penetration thicknesses derived from Eq. (3) based on the normalized images in Fig. 5. It can be seen that there will be a 10%–20% deviation if simply using the exponential law. After considering the energy spectrum, the deviation was eliminated and the results show precise thickness profiles as the real sample thickness.

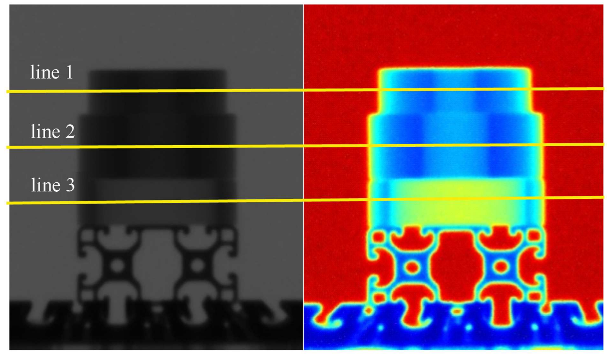

Fig. 5. (color online) Image of sample group 1 and data analysis lines. Left: radiographic image. Right: normalized image.

3 Neutron scattering effects

3.1 Point Scattered Functions (PScF)

Unlike the PSF (Point Spread Function) that used to describe the whole projection of a point in the specimen, PScF (Point Scattered Functions) is used to describe the density distribution of scattered neutrons on the detector from a point neutron source hitting directly to the material [14]. In brief, PScF records all the scattered neutrons that are not along the beam line, as shown in Fig. 7.

The PScFs of fast neutrons were simulated by the Monte Carlo program MCNPX on Linux cluster at the Leibniz Rechenzentrum [15]. To obtain the PScF data for a 10 cm thickness polyethylene with an error less than 5%, a number of 10^8 neutrons were simulated, which takes about 10 h with 64 CPUs parallel computing.

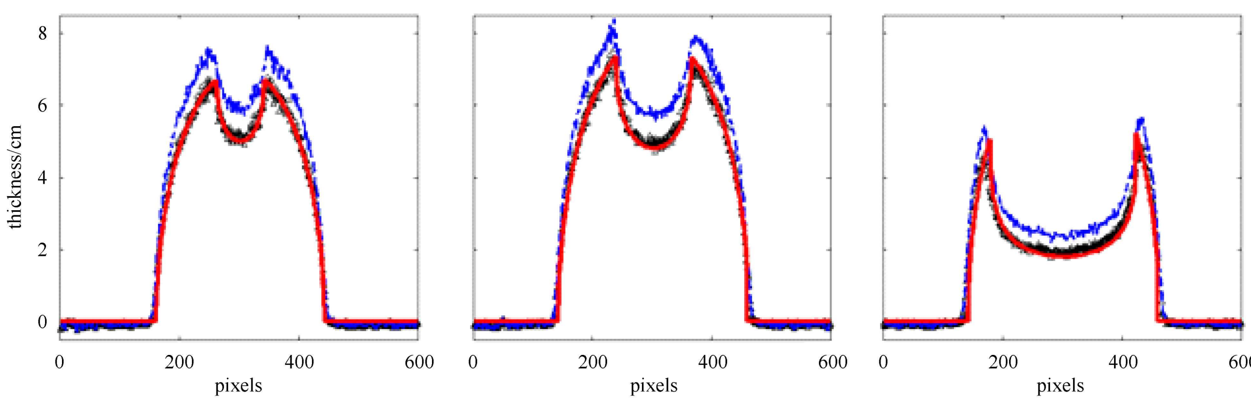

Fig. 6. (color online) Thickness profiles at different sample positions in Fig. 5. by different analysis method. (Left: line1. Middle: line2. Right: line3) Blue dashed line: Before energy spectrum correction. Black dotted line: After energy spectrum correction. Red solid line: Real thickness.

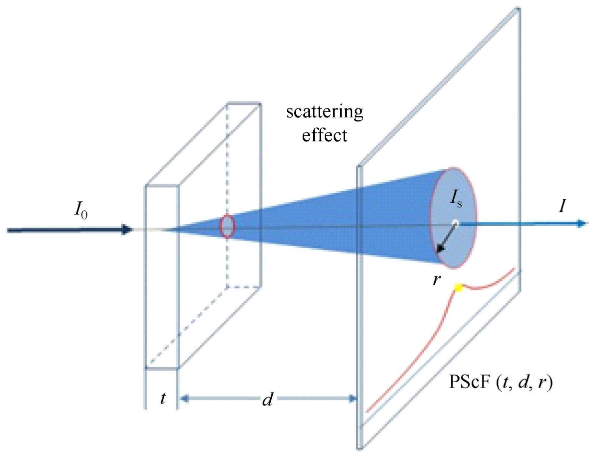

Fig. 7. (color online) The diagram of PScF of a neutron beam as a function of t,d,r.

The simulation parameters were set as follows. The geometry arrangement of NECTAR was based on the work of Harald Bretkreutz in his Ph.D. diploma thesis [16]. The neutron source is carried out as a 15 cm×15 cm area source with each point an isotropic divergence point source. The energy spectrum of each point source was characterized by the neutron spectra in NECTAR with energy range from 0.001 eV to 14 MeV [12]. As a simplification, we ignore the filters in the geometry layout. The fast neutrons are collimated and scattered by the architectures and finally arrive at NECTAR. The detector was described by a 40 cm-radius mesh tally with a series of rings. Each ring has a radius interval of 0.1 mm. Neutrons scattered into the rings will be counted and converted to the PScF density distributions on the detector. Different sample materials, thickness t and sample-to-detector distance d were set and simulated.

Figure 8 and Fig. 9 show the simulated PScFs for polyethylene with different sample thicknesses t and sample-to-detector distances d. It can be seen from Fig. 8 that with the increase of d, the scattering effect becomes weaker. Analytically, $S(d,t)$ has an inverse proportional relationship with the square of d for thermal neutrons [10]. Scattering effects can be ignored when the distance is larger than 100 mm. Unfortunately the increase of d would increase the geometric sharpness and reduce the resolution of radiography images. On the other hand, Fig. 9 shows that when the sample thickness becomes thicker, the scattering effects will increase first and then decrease. This can be explained by the fact that in thicker samples many scattered neutrons are multiply scattered and vanished inside of the sample instead of escaping and being detected.

For the mathematical application of the PScF, Gaussian functions and isotropically scattered functions were used to fit the PScF functions for thermal neutrons [10, 11]. In this work, the simulated PScFs were well described by the following function with a very good agreement:

$$\mathrm{PScF}(d,r)=\frac{S(d,t)}{\left(d^2+r^2\right)^2}, \tag{4}$$

where t is the thickness of the sample, d the sample-to-detector distance, r the radial distance and $S(d,t)$ a polynomial expression of t and d. The analytical functions of PScFs for polyethylene with different thicknesses and different sample-to-detector distances were also shown in Fig. 8 and Fig. 9. The results show good corresponding to the simulated data with the deviations less than 3%.

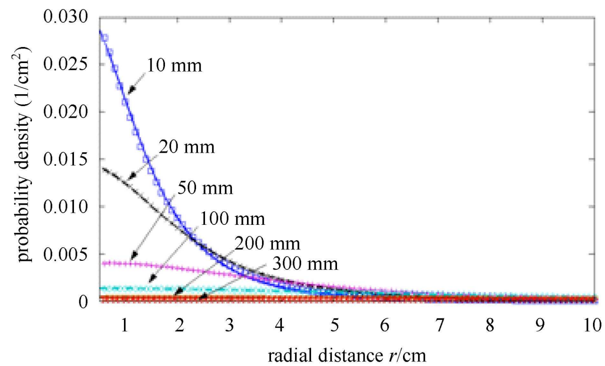

Fig. 8. (color online) MCNPX simulated PScFs for polyethylene with thickness 20 mm and different sample-to-detector distances.

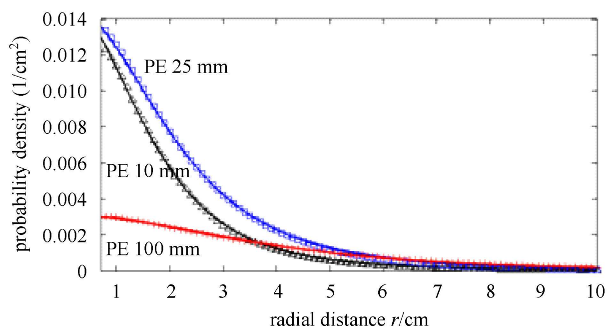

Fig. 9. (color online) MCNPX simulated PScFs for PE for sample-to-detector distance 20 mm and different thicknesses.

3.2 Correction procedure

The correction procedure was performed as follows:

1) Deriving the thickness distributions of the sample from radiography images considering the neutron spectrum effects initially;

2) Calculating the total scattering component I_s by a convolution of PScFs for each neutron beam in sample area based on PScF values;

3) Obtaining the corrected radiography image by a subtraction of initial image and scattering component I_s as shown in Fig. 10.

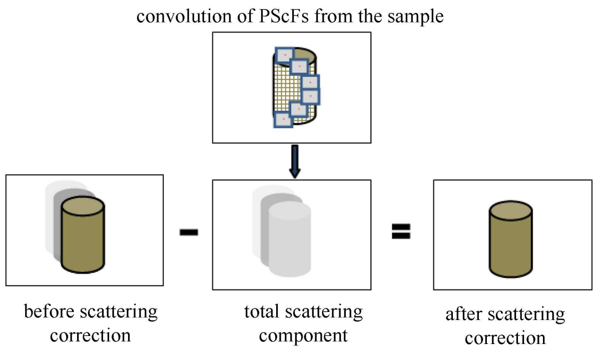

Fig. 10. (color online) Procedure of scattering corrections using PScF.

The whole scattering correction algorithm was implemented in a MATLAB code.

3.3 Experiments and results

Three bricks made of polyethylene and aluminum were used for scattering corrections. The first is a 152 mm×100 mm×25 mm polyethylene brick, the second is a 152 mm×100 mm×40 mm aluminum brick, and the third is a composition of PE and Al with thickness 100 mm, as shown in Fig. 11. The d from the back side of the samples to the fast neutron detector was: 10, 20, 50, 100, 200 and 300 mm respectively.

The preprocessed radiographic images of sample group 2 are shown in Fig. 12, Fig. 13 and Fig. 14(a). It can be seen that the radiographs and related intensity profiles have sensitive responses with d. Fig. 12, Fig. 13 and Fig. 14(b) show that scattered neutrons will make an extra contribution of 29% for PE and 53% for Al in the intensity profiles when d is small, which would yield a big error in the information estimation of the sample from exponential attenuation law. The smaller d is, the larger the deviation will be. When d is larger than 300 mm, the intensity profiles will be convergent and the scatterings from the object can be ignored.

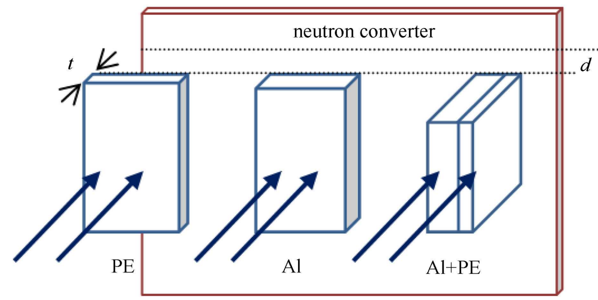

Fig. 11. (color online) Experiment diagram of sample group 2. Three samples are used: PE (t=25 mm), Al (t=40 mm), a composition of PE+Al (t=100 mm). The sample-to-detector distance d is changeable.

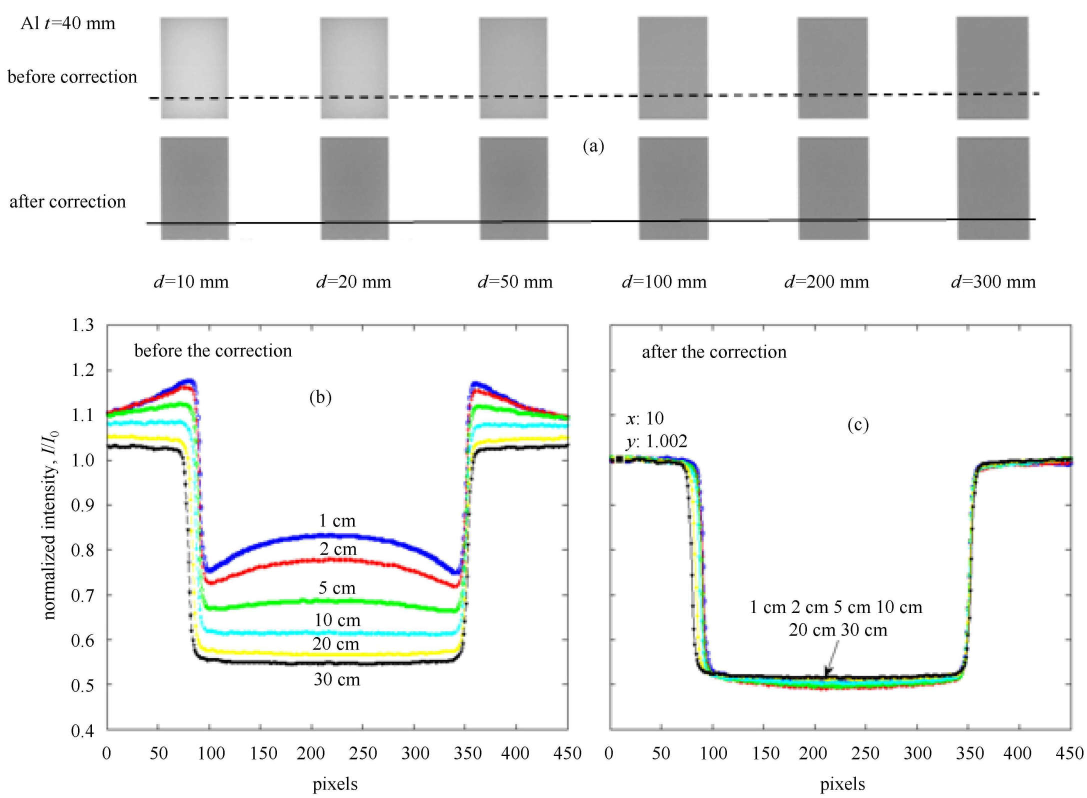

Fig. 12. (color online) (a) Uncorrected and corrected radiographic images of Al for different d. The intensity profiles of the dashed line for (b) the uncorrected radiographs and (c) for the corrected radiographs.

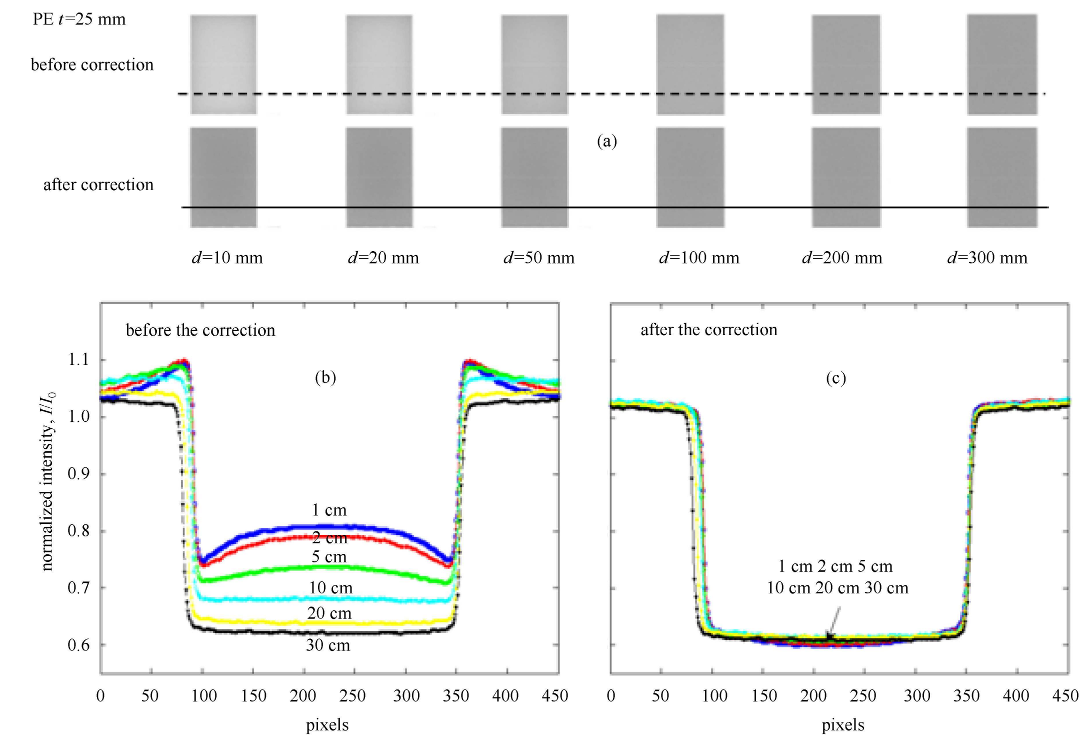

Fig. 13. (color online) (a) Uncorrected and corrected radiographic images of PE for different d. The intensity profiles of the dashed line for (b) the uncorrected radiographs and (c) for the corrected radiographs.

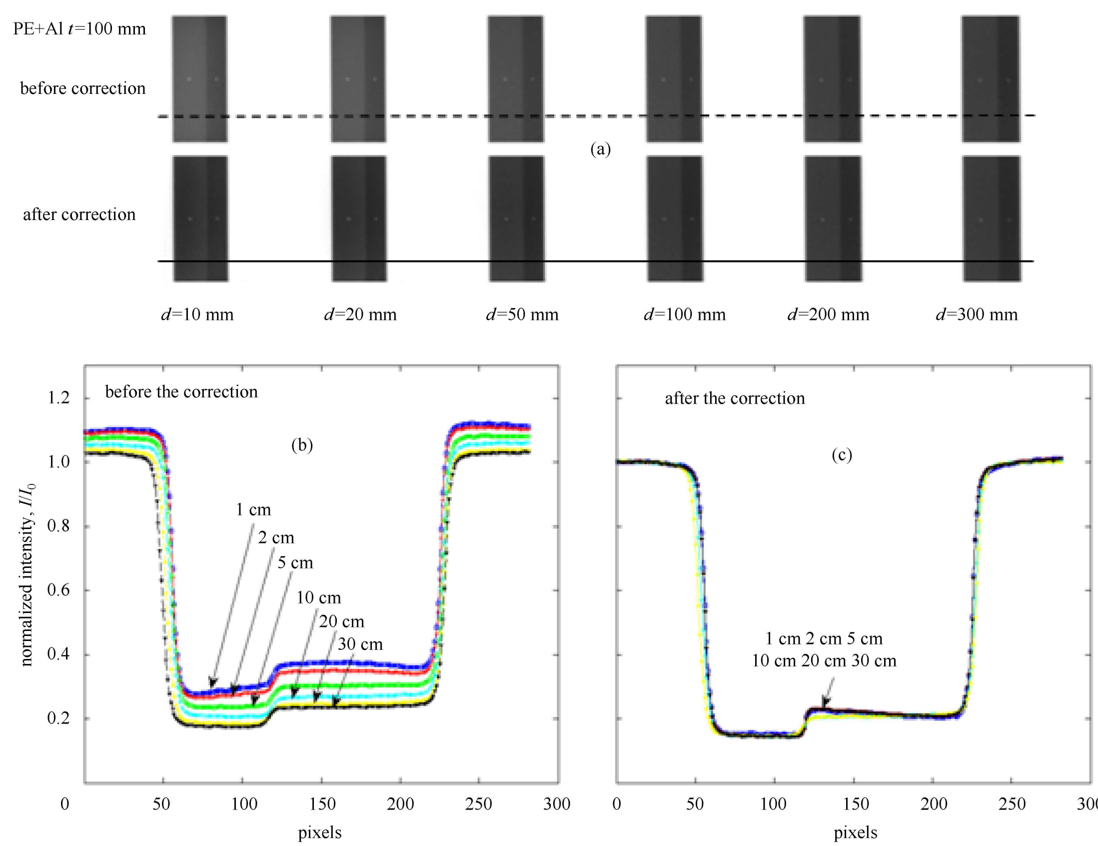

Fig. 14. (color online) (a) Uncorrected and corrected radiographic images of PE+Al for different d. The intensity profiles of the dashed line for (b) the uncorrected radiographs and (c) for the corrected radiographs.

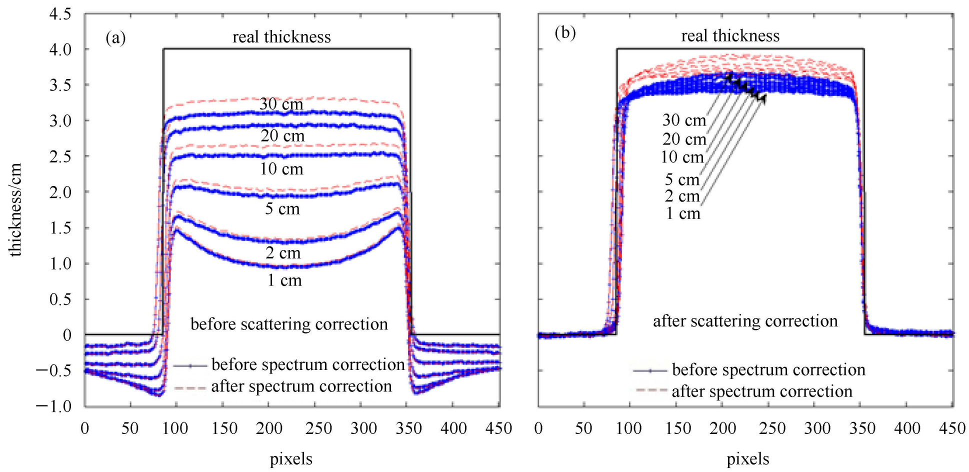

Fig. 15. (color online) Thickness distributions of 4 cm Al derived from the intensity profiles for different d. (a): Before scattering corrections. (b): After scattering corrections. Bold lines: Considering the energy spectrum. Dashed lines: Not considering the energy spectrum.

It can be seen in Fig. 12, Fig. 13 and Fig. 14 that after the scattering correction the artifacts caused by scattered neutrons disappear. The normalized intensity profiles are now independent of the sample-to-detector distance d. Maximum improvements of 63% for Al, 34% for PE and 65% for PE+Al were achieved after applying the PScF scattering corrections. As an examination of quantitative analysis results, corrected images of 4 cm Al were used to derive the thickness distribution of different d before and after the scattering corrections, with and without considering the neutron spectrum effects. The results are shown in Fig. 15.

It can be seen that the use of scattering corrections made a good improvement of the quantitative evaluation from the radiography images. Before the scattering correction, deviations from the obtained images are 33%–75% even considering the spectrum effects. After the scattering corrections, deviations reduce to 8%–15% for different d. Considering the energy spectrum of NECTAR, these deviations have a further reduction with an additional image improvement of about 5.5%.

4 Conclusion

For quantitative analysis and usage of fast neutron radiography in NECTAR, incident neutron spectrum and scattered neutrons from the sample are verified and corrected. Relationships of neutron transition intensities and penetration depths based on NECTAR spectrum were calculated and fitted for corrections. PScFs of fast neutrons for different materials were simulated and then fitted by analytical representations for further evaluations. A scattering correction algorithm was coded to evaluate the scattering components of the radiographic images. After eliminating the scattering components, the corrected images show identical and accurate results. For verification, intensities of 4 cm-Al before and after both corrections were compared and an improvement of 31%–65% was obtained for different sample-to-detector distances.

This work has been supported by the Academic Exchange Fund of Peking University Graduate School.

References

1 TANG Bin, ZHANG Song-Bao. Nuclear Electronics & Detection Technology, 2003, **23**(2): 176 (in Chinese)
2 Richards W J et al. Applied Radiation and Isotopes, 2004, **61**: 551
3 TANG Bin. Nuclear Electronics & Detection Technology, 2004, **24**(4): 387 (in Chinese)
4 Nalcioglu O, LOU R Y. Phys. Med. Biol, 1979, **24**(2): 330
5 Incident Neutron Data, ENDF/B-Ⅶ
6 DOU Hai-Feng, TANG Bin. CPC (HEP & NP), 2011, **35**(5): 483
7 CHEN Liang et al. Nuclear Physics Review, 2006, **23**(3): 310 (in Chinese)
8 ZHANG Fa-Qiang et al. Acta Physica Sinica, 2007, **56**(6): 3577 (in Chinese)
9 Yoshii Koji et al. Nucl. Instrum. Methods A, 1996, **377**: 76
10 Hassanein R et al. Nucl. Instrum. Methods A, 2005, **542**: 353
11 Kardjilova N et al. Nucl. Instrum. Methods A, 2005, **542**: 336
12 Bücherl T et al. Nucl. Instrum. Methods A, 2011, **651**: 86
13 GUO J et al. Nucl. Instrum. Methods A, 2009, **605**: 69
14 Hecht E. Optik. Bonn Munich, Addison-WesleyPublishing CompanyInc., 1989
15 http://www.lrz.de/services/compute/linux-cluster/doc/860-0237-001.pdf
16 Breitkreutz Harald, Spektrale Charakterisierung des Therapiestrahlsam FRM II (Ph. D. thesis). Munich: Fakultätfür Physik, Technische Universität München, FRM II, 2007 (in German)